Harnessing post-buckling deformation to tune sound absorption in soft Helmholtz absorbers

Nan Gao [a], Sichao Qu [a], Jian Li [b], Jiao Wang [b,c,*], Weiqiu Chen [b,d,*]

[a] Department of Physics, The Hong Kong University of Science and Technology, Clear Water Bay, Hong Kong, China
[b] Key Laboratory of Soft Machines and Smart Devices of Zhejiang Province & Department of Engineering Mechanics, Zhejiang University, Hangzhou 310027, China
[c] Department of Civil Engineering, Zhejiang University, Hangzhou 310058, China
[d] Soft Matter Research Center, Zhejiang University, Hangzhou 310027, China

ARTICLE INFO

ABSTRACT

Helmholtz resonator (HR) has always been an important part of artificial sound-absorbing materials, most of which however cannot be tuned in real time and hence have a limited scope of applications. In this work, we integrate for the first time the soft hyperelastic material into the main structure of HR to design a star-shaped soft Helmholtz absorber. The soft HR exhibits different post-buckling deformation behavior when its wall-thickness varies, which further yields different acoustic characteristics. By combining two star-shaped HRs with different wall-thickness, we are able to achieve asymmetric sound absorption when specific and respective compression loads are applied to the two HRs. In addition, high sound absorption at various frequencies can be obtained via different combinations of the applied loads. Due to the perfect capability of reversible large deformation of soft hyperelastic materials, the sound absorption of the proposed pair of HRs can be real-time tuned effectively by mechanical loading and unloading. In other words, the acoustic switch controlled by mechanical load can be realized. The proposed soft absorber has an obvious practical application value, and also provides an important illustration for the design of soft and tunable acoustic devices.

1. Introduction

Sound absorption has always been a very traditional subject. The appearance of acoustic metamaterial absorbers however remediates the problems, such as heavy, low efficiency and high price, that are usually associated with the traditional sound-absorbing materials (e.g., sponge, glass fiber, porous polymer material) [1,2]. For the sound wave in the low-frequency range, whose wavelength is relatively large, a traditional way is to use a large-scale material to obtain a high absorption. However, an acoustic metamaterial absorber can be made in a sub-wavelength size with high absorption due to its fantastic microstructure. Thus, using metamaterial absorbers can reduce the space while improve the efficiency of sound absorption [3–7]. Hence, acoustic metamaterial absorbers are now widely used in the field of noise reduction. For a perfect sound absorber, there are two key factors that need to be considered. The first is the impedance matching mechanism. The surface impedance of the absorber needs to match the air impedance to make the sound wave enter the absorber more effectively [8]. The other thing is the energy dissipation. High sound absorption can be achieved by improving the energy density of the whole system or using the reverse action of correlation waves. The dissipation of energy is the volume integral of the product of local energy density and dissipation coefficient so that the dissipation can be enhanced by increasing the energy density. Because the energy density is related to the displacement velocity of particles, the local resonance can effectively enhance the energy density and further improve the sound absorption ability. Based on the understanding of these two points, many acoustic metamaterial absorbers have been designed, including Helmholtz resonators (HRs) [9–11], membrane type acoustic metamaterials (MAMs) [12–16], hybrid membrane resonators (HMRs) [17–19], Fabry-Perot (FP) absorbers [20-22], ultrathin metamaterial absorbers [23,24], hybrid composite absorbers [25] and some others [26–28]. Among them, Fu et al. [29] put a pair of HMRs composed of two decorative membranes and back cavities on the side of the waveguide, and designed a metamaterial which can achieve sound absorption at single frequency. On this basis, Long et al. [30] replaced HMR with HR to achieve perfect sound absorption. In addition, based on the design strategy through the combination of resonators with different resonance frequencies, broadband sound absorption could be realized. For example, in view of the causality principle, Yang et al. [24] combined FP resonators with a power-law arrangement of the resonance frequencies, and found that broadband sound absorbers could be obtained with the thinnest material. After that, Jiménez et al. [31]

designed a deep-subwavelength structure with HRs to achieve broadband sound absorption. Furthermore, the combining utilization of various optimization algorithms can lead to a wider frequency absorption effect [32] as well as the reverse design of sound-absorbing metamaterials [27].

For the single-port system, its exit end is a hard wall, that is, the entrance and the exit of the system share the same port. Such a system is therefore unventilated. In order to meet the needs of a wide range of practical applications, the double-port system or some ventilated acoustic absorbers have gradually become the focus of research in recent years [29,30,33]. For example, Xiang et al. [34] designed an ultra-open ventilated metamaterial sound absorber for low frequency sound below 1kHz, and realized broadband sound absorption by using the combination strategy. Xu et al. [35] designed a broadband ventilated acoustic barrier via combining the bandgap properties of periodic structure with topology optimization, demonstrating the effect of broadband sound insulation. Compared with the closed system, the ventilated sound absorber has a broader application value [33,36–39]. It can be used to reduce the noise inside the pipes, or indoor noise, so that the application scenarios can be more diverse. Some works have shown that asymmetric or high ventilation absorption can be achieved in a two-point system composed of MAMs, HMRs or HRs. However, the ventilated sound-absorbing metamaterials reported in the literature are all made of hard materials (metal or plastic) or membrane materials. Due to the relaxation of the membrane under a constant tension, the absorber composed of the membrane (MAMs, HMRs) is not stable for a long-term service. On the contrary, the HR is more stable, whose overall loss can also be adjusted by changing its geometric parameters, making it more robust than the absorber composed of membranes. Therefore, this work aims to design a ventilated absorber based on the structure of HR. It is worth noting that, although hard materials as employed in the existing ventilated HR metamaterials have a long service life, their mechanical characteristics (in sound-related applications, the geometry or configuration of the structure is the most important) cannot be changed flexibly in real time. Once the configuration of the absorber is determined, the corresponding absorption frequency and absorption capability are also determined, which may limit the application spectrum of hard HR absorbers.

This difficulty may be surmounted by using soft materials. Due to the characteristic of large and reversible deformation, soft materials are widely used in the field of metamaterials, especially in the light of mechanical control [40–44]. For example, the elastic band gaps in soft periodic structures can be tuned by mechanical loading which can change both the topological configuration and the effective material properties [41,43,45–48]. Gao et al. [42] have experimentally demonstrating the real-time tuning of elastic band gaps in soft phononic crystals with criss-crossed elliptical holes via a tensile load. It is also possible to produce special transmission phenomena, such as topological interface state [49], elastic wave guide [50,51] and many others [52–54], in some specially designed soft (dielectric) phononic crystal structures by mechanical loading or electric means. It is worth mentioning that the designed soft material structure will enter into the stage of buckling/post-buckling deformation under a certain mechanical loading. At such stage, the initial configuration of the structure will change greatly, the introduction of a small geometric defect or simply the change in a geometric parameter (such as the thickness) of the initial configuration may cause different post-buckling deformations, which provides the possibility of rich geometry configurations for further realizing interesting acoustic functionalities [55,56]. Therefore, it is very interesting and also important to realize the reversible mechanical control of the structure by making use of the particularity of soft materials.

In this paper, we design a star-shaped Helmholtz absorber by integrating the soft material with HR, and adjust its thickness to obtain different post-buckling deformations. Combining with star-shaped HRs with different thickness, and making use of change in effective geometric parameters (such as volume, effective height and cross-sectional area) induced by different post-buckling deformations, we can achieve perfect sound absorption and asymmetric sound absorption at different frequencies. The feasibility of this design is confirmed by theory and finite element (FE) simulation. Compared with the traditional HR absorbers, our design can flexibly tune the sound absorption frequency and absorption coefficient by mechanical loading, which gives a brilliant illustration of the design of a broad spectrum of soft acoustic devices.

2. Design principle

It is well known that if the vertical plate with its bottom edge fixed and the top hinged is subjected to a downward compression load, it will deform within its middle plane at first. But when the load arrives at a certain critical value, the plate will buckle, and further increasing the load will make it bend and enter into the post-buckling deformation state, as shown in Fig. 1(a). For a thin plate made of soft hyperelastic material, the post-buckling deformation is reversible due to the excellent elasticity of the material. Therefore, we use rubber (soft material) to make the cavity part of a HR, which can undergo reversible deformation under mechanical loadings. In addition, in order to enrich the post-buckling deformation configurations of the whole structure, the cross section of the cavity is designed to be star-shaped so that each side wall is composed of two thin plates.

The star-shaped HR consists of two parts: the rubber side walls of the cavity and the hard base with a thin neck, as shown in Fig. 1(b). The inner height of the cavity (air part) is $H=5 \times 10^{-2}$m, while the inner diameter and height of the neck are $2r = 12 \times 10^{-3}$m and $h = 11 \times 10^{-3}$m, respectively. The thickness of the cavity is t, the length and width of the outer cross section are both L, the length and width of the inner cross section are both $l = 5 \times 10^{-2}$m, and the corner angle is $\theta = 78.6°$. In order to explore the influence of mechanical loading on the post-buckling deformation of the star-shaped HR, the Explicit module of the FE software ABAQUS is used for simulation [57,58]. For this purpose, the incompressible Neo-Hookean hyperelastic model [41] with density $\rho_{rubber} = 1080$ kg/m^3, Young's modulus $E = 8 \times 10^6$ Pa and initial shear modulus $\mu_0 = 1.34 \times 10^6 Pa$ are employed. In order to improve the computational efficiency, the 4-node shell element (S4) is used in ABAQUS model meshing. It is noted here that, because the thickness of the structure t used is 4 or 5×10^{-3}m, which is less than 1/10 of the overall size, and the deformation of the structure is mainly bending, using the shell element without considering the transverse shear deformation is sufficient to meet the computational accuracy. Without loss of generality, displacement loading is adopted in the FE simulation, which is measured by the nominal strain defined by $\varepsilon = \Delta u/H$ (Δu is the amount of deformation along the loading direction and the positive sign represents compression, while H is the initial height of the air cavity along the loading direction).

It should be noted here that, with the above material parameters, the characteristic impedance of the soft material can be calculated as,

$$Z_{rubber} = \rho_{rubber}c_{rubber} = \sqrt{\rho_{rubber} \times K_{rubber}} \approx 890 \times Z_0 \tag{1}$$

where K_{rubber} is the bulk modulus of the rubber, and Z_0 ($= \rho_0 c_0$) is the characteristic impedance of air, which is equal to the product of air density and sound speed. The characteristic impedance of rubber is about 890 times of the air, which means the impedance difference between the two is very large. Therefore, the inner wall of the soft material can be regarded as an acoustically rigid wall. In this case, we can only consider the influence of the deformation caused by the buckling of the wall and can neglect the vibration effect of the material that might be induced by the sound. However, if the characteristic impedance is close to the air, both effects should be taken into consideration, i.e. a fully-coupled model should be established [59].

For the star-shaped cavity of the HR made of rubber, we can fix its bottom and apply a compressive load on its top, as shown in Fig. 1(c). The load will induce the post-buckling deformation of the side walls, which further affects the overall acoustic characteristics of the HR. In
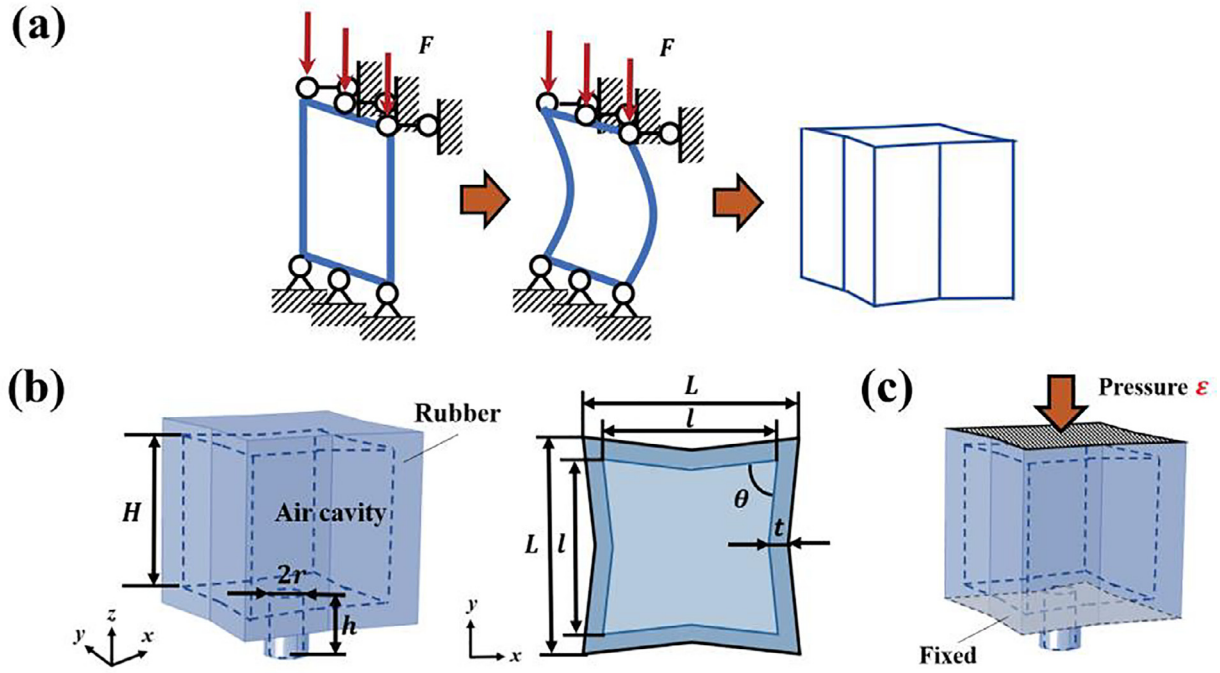
Fig. 1. Design of a star-shaped HR: (a) Basic principle; (b) Geometric parameters, including inner height of the cavity ($H = 5 \times 10^{-2}$m) and the neck ($h = 11 \times 10^{-3}$m), inner radius of the neck ($r = 6 \times 10^{-3}$m), thickness of the cavity (t), side length of the outer (L) and the inner ($l = 5 \times 10^{-2}$m) cross sections, and the corner angle ($\theta = 78.6°$); (c) Applied load and boundary conditions.

this regard, the acoustic characteristics of the designed HR can be tuned by mechanical loading. Moreover, if the post-buckling deformation configuration is abundant, such means of mechanical tuning will be very flexible and efficient.

3. Two distinct post-buckling configurations

The thickness of the plate will affect its buckling deformation. We now consider two kinds of cavities with different wall thickness to realize the post-buckling deformation with different topological configurations. Based on the simulation results shown in Fig. 2(a), it can be noted that, when the wall thickness is 4×10^{-3}m, the cavity mainly experiences two deformation modes when the compression load is applied to its top. The first one (Mode 1-I) is characterized by no obvious deformation of its side walls, and only occurs in the early stage of loading, i.e. when the compression load is small. With the increasing of the compression, the phenomenon of mode jump is observed, from the overall shape-keeping mode to the other mode (Mode 1-II) with two opposite side walls concave and the other two convex, as shown in Fig. 2(b). When the wall thickness of the cavity is 5×10^{-3}m, the modes will be interestingly different. In the case of small compression, the mode 2-II is similar to that of Mode 1-I, with no obvious deformation of the side walls and hence no obvious change in the shape. When the degree of compression increases, mode jump also appears, but the mode (Mode 2-II) is different from the 4×10^{-3}m case with all the four deformed walls convex, as shown in the figure. Different wall thicknesses bring about different post-buckling deformation configurations after the mode jump under the same compression load, which is critical to the subsequent tuning of the acoustic characteristics.

For a HR, the volume and height of the cavity are two very important parameters, which will directly affect its resonance frequency. In fact, the control of acoustic characteristics via post-buckling deformation is also based on this principle, which is the basis of our design. Hence, we numerically examine the change in cavity volume for the two HRs with different thickness under the same compression, as shown in Figs. 3(a) and (b). It can be noted that, for the case of $t = 4 \times 10^{-3}$m, the cavity

volume decreases with the increase of the compression load. After the point of mode jump where $\varepsilon = 4.4\%$, the cavity volume will first increase slightly, but soon it will decrease again with the compression load. For the case of $t = 5 \times 10^{-3}$m, the situation is quite different: the volume first decreases slightly, then increases after a critical value of the load, and finally decrease again after a second critical value of the load. The volume change in the first stage is similar to the case of $t = 4 \times 10^{-3}$m, proving that the first-stage deformations (Mode 1-I and Mode 2-I) are similar to each other when the HR is compressed. When the load reaches a critical value $\varepsilon = 4.4\%$, the second-stage mode changes from Mode 2-I for the case of $t = 4 \times 10^{-3}$m to Mode 2-II for the case of $t = 5 \times 10^{-3}$m. In the latter case, the cavity volume increases with the load in the second stage. However, after the second critical load $\varepsilon = 13.9\%$, the volume increase due to the bulge of the side walls cannot make up for the volume loss due to the whole shortening. Thus, the cavity volume decreases again with the load in the third stage. It should be noted that the observed post-buckling deformations of the soft HR with two different thicknesses are only for the case that its bottom is clamped and its top is uniformly compressed. If the structure is loaded unevenly, other post-buckling modes would be possible. Fig. 3 also depicts the variation of the strain energy (black dashed line) and that of the kinetic energy (grey dashed line). It can be found that with the increase of the compression load, the strain energy increases approximately linearly. Meanwhile, the kinetic energy, which is caused by the loading mode adopted in the simulation, is far less than the strain energy so that the loading process keeps to be quasi-static.

In order to verify the reliability of the simulation results in ABAQUS/Explicit, the buckling analysis of soft HR with two wall thicknesses is carried out in ABAQUS/Standard. The results show that, the buckling modes and critical loads obtained by the Standard module are very close to those by the Explicit module. The reader is referred to Appendix A for the details.

Combining these two HRs with different thickness, we can achieve a flexible mechanical control of some acoustic phenomena at certain frequencies. Moreover, due to the resilience of soft hyperelastic materials and their large deformation capability, the control is reversible,
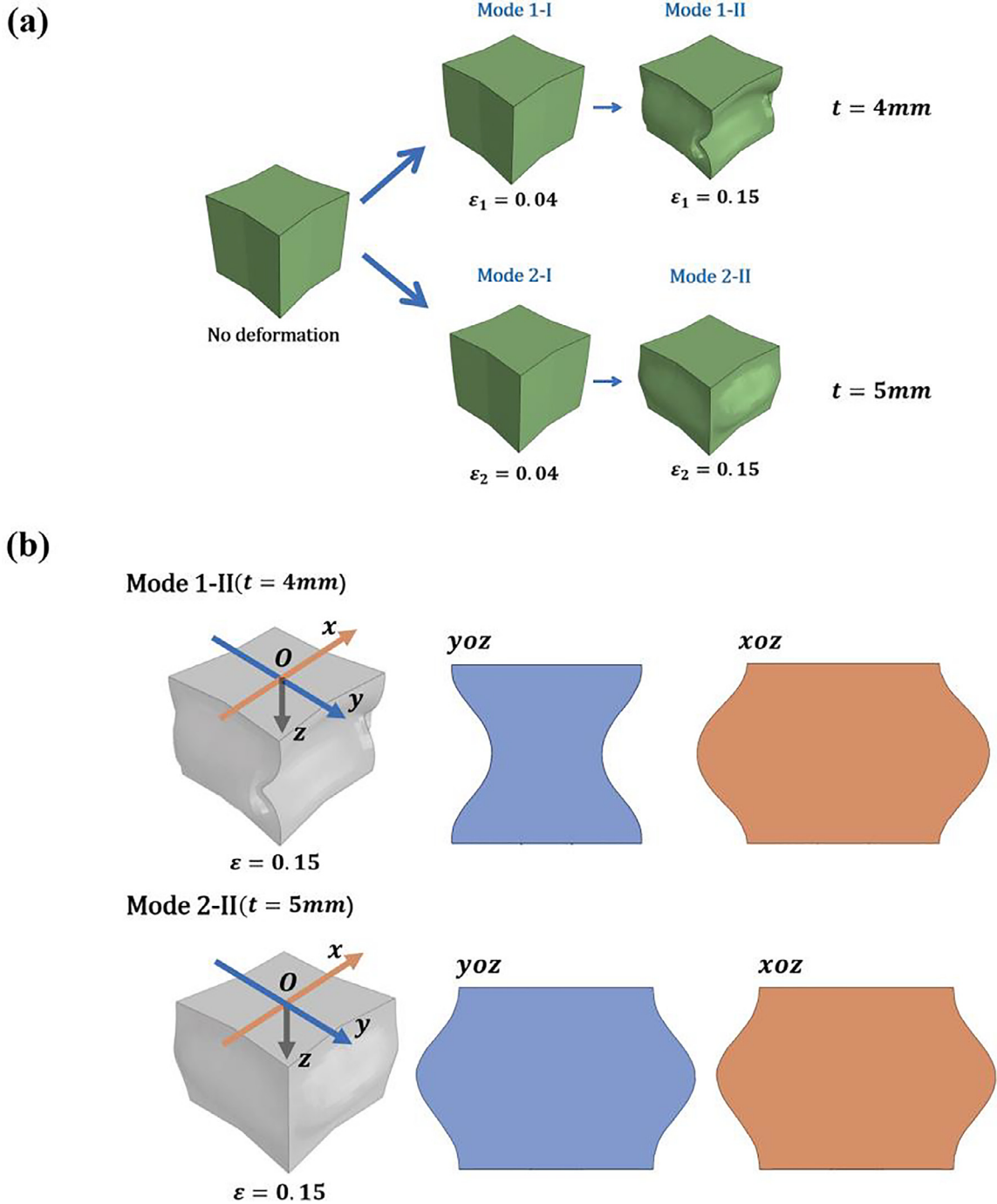
(a)

(b)

Fig. 2. Two distinct post-buckling configurations: (a) Shapes of the deformed HR for two thicknesses for which the first mode jump occurs when ε is around 0.04; (b) When $t = 4 \times 10^{-3}$m, the two opposite side walls are concave, and the other two are convex, while for $t = 5 \times 10^{-3}$m, all the four side walls are convex.

repeatable and of wide range, differing from the traditional Helmholtz absorber that is made of hard materials.

4. Theoretical basis for the HR absorber

Consider the equivalent impedance of a single star-shaped HR firstly. The star-shaped HR consists of a cavity and a narrow neck, with their heights being H and h, respectively. Denote A_c and A_n as the cross-section areas of the cavity and the neck, respectively. In order to simplify the calculation, the cross-section area of the cavity here is the effective one, defined by $A_c = V_c/H_c$, where V_c and H_c are the volume and height of the cavity, respectively, both varying with the load.

According to the duct-acoustics theory[60], the effective dynamic density and effective modulus are given by

$$\rho_j(\omega) = \rho_0 \left(1 - i \frac{\delta}{2\Lambda_j} \right),$$

$$B_j(\omega) = B_0 \left(1 + i \frac{\delta}{2\Lambda_j} \frac{\gamma - 1}{\sqrt{\mathrm{Pr}}} \right), \qquad (2)$$

where $\Lambda_j = V_j/S_j$ is the characteristic length (the subscript $j = n$ or c to denotes the neck or cavity respectively), S_j is the side surface of the duct (neck or cavity), which is approximately a constant, and V_j is its volume. The energy dissipation of HR is mainly due to the vis-
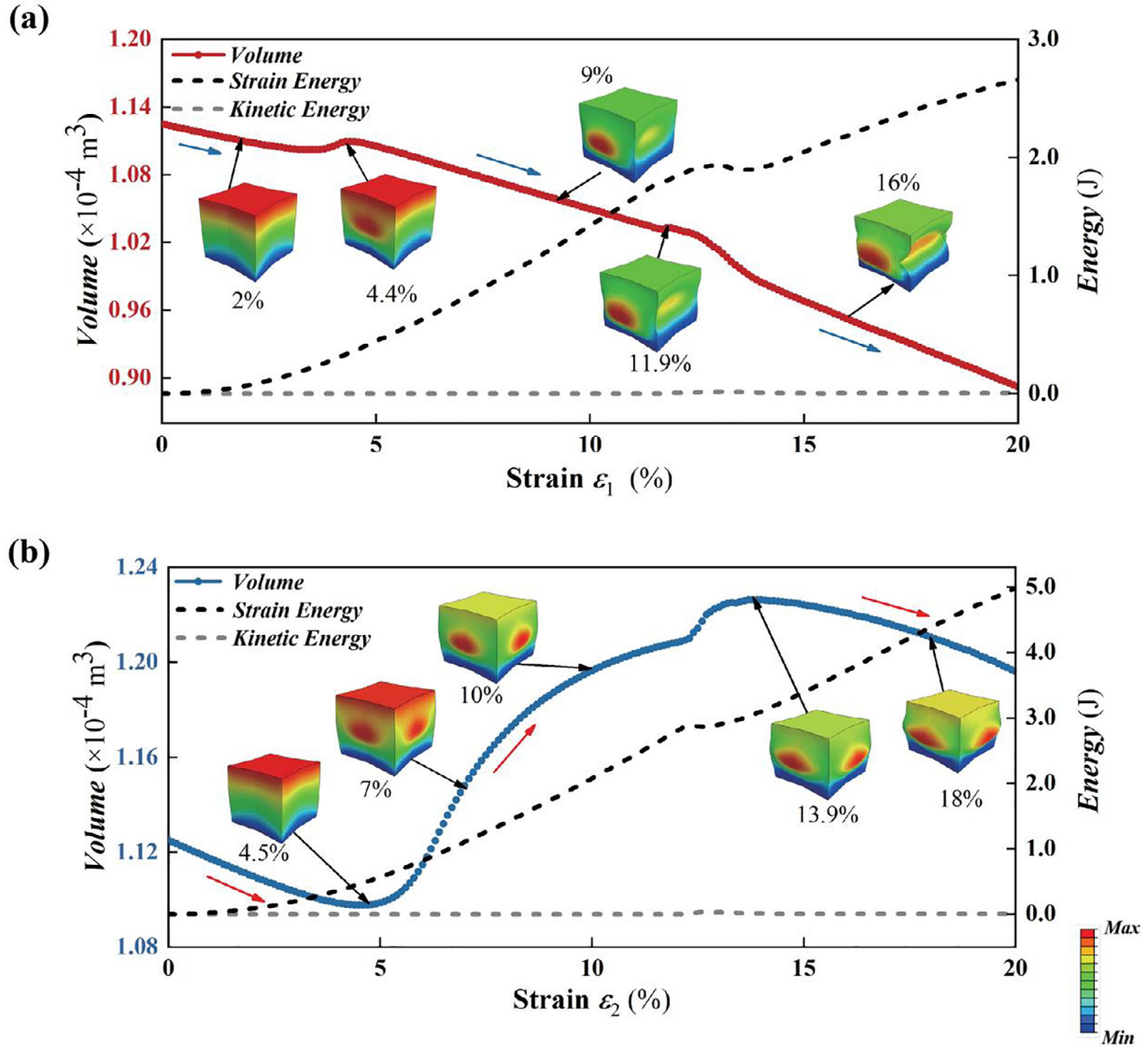
Fig. 3. Variations of the cavity volume (solid line), the strain energy (black dash line), and the kinetic energy (grey dash line) with the compression load applied on the HR with different thickness: (a) $t = 4 \times 10^{-3}$m; (b) $t = 5 \times 10^{-3}$m. The color represents the magnitude of the displacement, with red and blue corresponding to the maximum and the minimum, respectively.

cous friction between the air and the inner wall surfaces of the neck and cavity, which needs to be considered. In Eq. (2), the viscous boundary layer $\delta = \sqrt{2v/\omega} \ll 2r$, the adiabatic index $\gamma = 1.4$ and the Prandtl number $\text{Pr} = v/\chi$, where ω is the frequency of the sound wave, the kinematic viscosity $v = 1.5 \times 10^{-5}$m^2/s and the thermal diffusivity $\chi = 1.9 \times 10^{-5}$m^2/s. The air density and modulus are $\rho_0 = 1.2$kg/m^3 and $B_0 = 141.2 \times 10^3$Pa, respectively. The above material constants can be found in Ref. [1]. Then, the effective impedance Z_j and wave vector k_j are given by

$$Z_j = \sqrt{\rho_j B_j}/A_j,$$
$$k_j = \omega\sqrt{\rho_j/B_j}. \tag{3}$$

According to the impedance transfer theory [60], the impedance of HR can be expressed as

$$Z' = -iZ_c \cot(k_c h),$$
$$Z_{\text{HR}} = Z_n \frac{Z' + iZ_n \tan\left[k_n(H + \Delta l)\right]}{Z_n + iZ' \tan\left[k_n(H + \Delta l)\right]}. \tag{4}$$

where the end correction [31] is made by adding a length Δl, which is related to the pressure radiation at the discontinuous interface. For a

HR placed on the side wall of a waveguide, there are two discontinuous interfaces, one is the interface between neck and cavity of HR, and the other is the interface between neck and waveguide. Therefore, the correction length Δl consists of two parts Δl_1 and Δl_2, the former is related to the configurations of neck and cavity [61], while the latter is related to the geometric parameters of neck and waveguide [62], which are given by

$$\Delta l_1 = 0.82\left[1 - 1.35\frac{r_n}{r_c} + 0.31\left(\frac{r_n}{r_c}\right)^3\right]r_n,$$

$$\Delta l_2 = 0.82\left[1 - 0.235\frac{r_n}{r_t} - 1.32\left(\frac{r_n}{r_t}\right)^2 + 1.54\left(\frac{r_n}{r_t}\right)^3 - 0.86\left(\frac{r_n}{r_t}\right)^4\right]r_n, \tag{5}$$

where the effective radii $r_c = \sqrt{A_c/\pi}$, $r_n = \sqrt{A_n/\pi}$ and $r_t = \sqrt{A_t/\pi}$ (A_t is the cross-section area of the waveguide). So the additional lengths at both ends are corrected as $\Delta l = \Delta l_1 + \Delta l_2$. In an acoustically resonant system with resonance frequency Ω, the surface response function (Green function) of a resonator can be expressed as
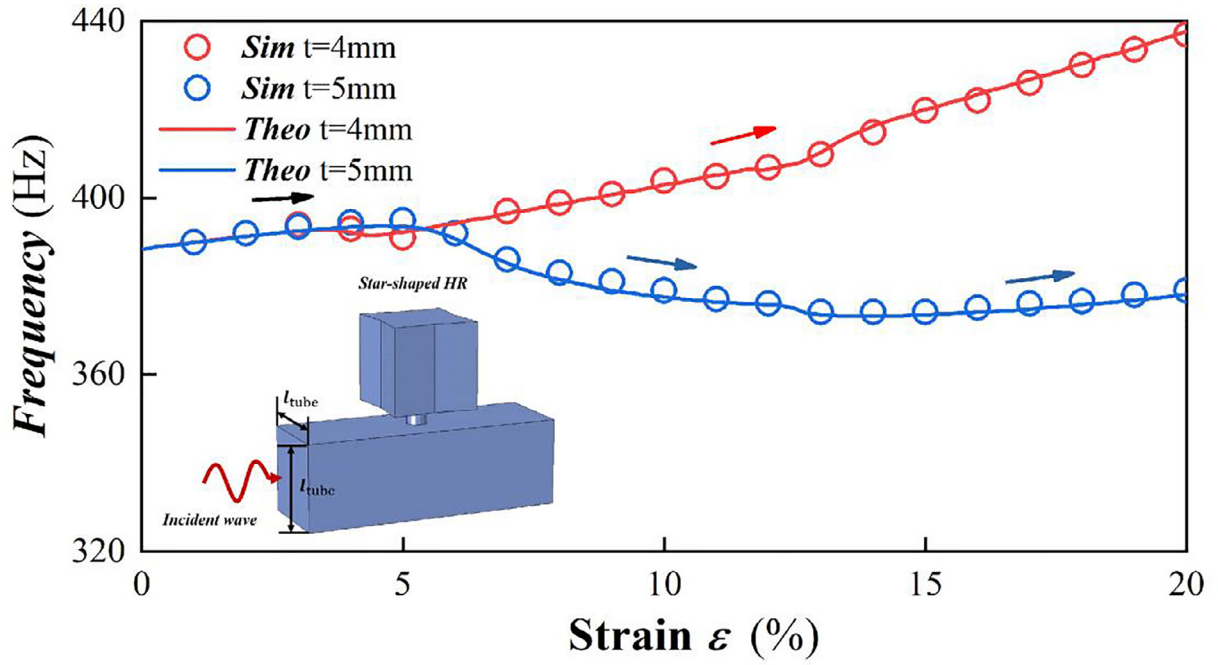
$$G = \frac{\xi}{p} \tag{6}$$

Fig. 4. Variations of the resonance frequency of a single star-shaped HR with the compression load. The circles are the FE results, and the lines are the theoretical results. The arrow represents the direction of change, and red and blue colors correspond to $t = 4 \times 10^{-3}$m and $t = 5 \times 10^{-3}$m, respectively. In the calculation, the length and width of the cross section of the uniform waveguide are both $l_{tube} = 5 \times 10^{-2}$m.

where p is the actual sound pressure and ξ is the magnitude of displacement response of the air particle. Because the impedance of the resonator can be expressed as

$$Z = \frac{p}{u} = \frac{p}{i\omega\xi} = \frac{1}{i\omega G} \tag{7}$$

Eq. (6) can be rewritten as

$$G = \frac{1}{i\omega Z} \tag{8}$$

For a plane wave in air, the real part of the Green function is non-dissipative, and its dissipative imaginary part Im(G)corresponds to the real part of the impedance Re(Z). Moreover, the function of G can be denoted as a Lorentz form, that is, at the resonance frequency, there will be a peak in the imaginary part, which means the dissipation reaches the maximum and Re(Z)is zero [63]. In view of this property, the resonance frequency of the star-shaped HR can be found at the position of the peak of Im(G), with G being calculated from the impedance:

$$G = \frac{1}{i\omega Z_{HR}} \tag{9}$$

We now use both the above theoretical formulae and the FE simulation to explore the influence of the compression load on the acoustic properties of the soft star-shaped HR. The model is shown in the Fig. 4, that it, a star-shaped HR is placed on the side wall of a uniform waveguide with the side length $l_{tube} = 5 \times 10^{-2}$m of the cross section, and the incident wave is incident from one end of the waveguide. The results are shown in Fig. 4.

It is noted that, the variation of the resonance frequency of the soft star-shaped HR with the compression load is basically consistent with the variation of the volume. When $t = 4 \times 10^{-3}$m, the resonance frequency of the HR increases with the increase of the load, and the resonance frequency ranges from 388Hz to 440Hz when ε varies from 0 to 0.02. Similarly, when $t = 5 \times 10^{-3}$m, the varying trend of the resonance frequency is also consistent with the volume, which first increases, then decreases, and finally increases. The frequency range is 373-394Hz, which is relatively narrow. However, the variation of the latter, which is not monotonic, is much richer than the former.

In order to design a ventilated and mechanically tunable sound absorption device, the star-shaped HR is mounted on the side wall of a waveguide. It should be noted that for the case of one beam incident wave, the absorption of an individual dipole or monopole will not exceed 50%, which has been proved theoretically [64]. Therefore, in order to obtain high absorption, two HRs need to be mounted on the side wall. As shown in Fig. 5(a), the system consists of a two-port waveguide and two star-shaped HRs. The geometrical parameters of the waveguide are consistent with those mentioned above, $l_{tube} = 5 \times 10^{-2}$m, and the distance d between the centers of the two HRs is 5.6×10^{-3}m. The wall thickness of the first HR on the left is 4×10^{-3}m, and that of the second one is 5×10^{-3}m. The compression loads applied on them are ε_1 and ε_2, respectively. When two star-shaped HRs are set on the side wall of the waveguide, the overall acoustic characteristics (reflection R, transmission T and absorption A) of this system can be calculated by the transfer matrix method [29]:

$$T_{all} = T_{HR1}T_{mid-tube}T_{HR2} \tag{10}$$

where the concrete forms of the contributing matrices are obtained by

$$T_{HRm} = \begin{bmatrix} 1 & 0 \\ 1/Z_{HRm} & 1 \end{bmatrix},$$
$$T_{mid-tube} = \begin{bmatrix} \cos(kl) & iZ_0\sin(kl) \\ i\sin(kl)/Z_0 & \cos(kl) \end{bmatrix}. \tag{11}$$

where $m = 1, 2$, representing the sequential number of the HR, T_{HRm} is the transfer matrix of the m-th HR and $T_{mid-tube}$ is the transfer matrix of the intermediate impedance tube between the two HRs (red shadow part in Fig. 5a). Then, we can get the reflectance and transmittance as follows:

$$R^+ = \left| \frac{-T_{11}+T_{12}/Z_0-Z_0T_{21}+T_{22}}{T_{11}+T_{12}/Z_0+Z_0T_{21}+T_{22}} \right|^2,$$
$$R^- = \left| \frac{T_{11}+T_{12}/Z_0-Z_0T_{21}-T_{22}}{T_{11}+T_{12}/Z_0+Z_0T_{21}+T_{22}} \right|^2, \tag{12}$$

$$T^+ = T^- = \left| \frac{2e^{ikL}}{T_{11}+T_{12}/Z_0+Z_0T_{21}+T_{22}} \right|^2, \tag{13}$$
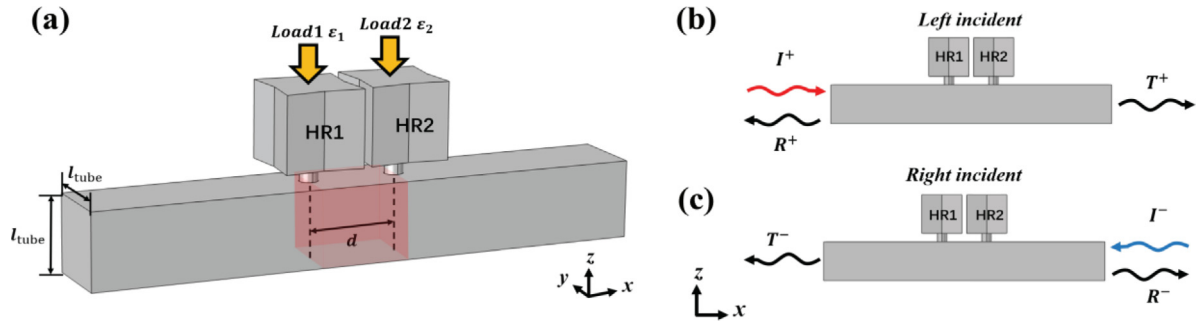
Fig. 5. Double star-shaped Helmholtz absorber: (a) Schematic diagram and some geometric parameters; (b) The incident wave is incident from the left side of the waveguide, and the superscript '+' is used in the corresponding acoustic parameters; (c) The incident wave is incident from the right side of the waveguide, and the superscript '-' is used in the corresponding acoustic parameters.

where T_{mn} ($m = 1, 2, n = 1, 2$) represent the elements of the total transfer matrix T_{all} in Eq. (10), the sign of '+' indicates that the incident sound wave incidents from the left side of the waveguide, as shown in Fig. 5(b), and the sign of '−' denotes the incident wave is coming from the right side of the waveguide, as shown in Fig. 5(c). R and T are the reflection and transmission coefficients, respectively. Then, according to the energy conservation principle, the absorptance can be obtained as

$$A^+ = 1 - R^+ - T^+,$$
$$A^- = 1 - R^- - T^-, \qquad (14)$$

where A is the absorption coefficient, and the superscript again corresponds to the incident direction of the incident wave.

5. Mechanically tunable sound absorber

Based on the theoretical basis presented in the previous section, asymmetric sound absorption and multi-frequency perfect sound ab-

sorption can be realized by applying different compression loads on the top of the two star-shaped HRs.

5.1. Asymmetric sound absorption

When certain compression loads are applied to the two star-shaped HRs, due to the different post-buckling configurations, the two cavities will experience different deformations, which further lead to an asymmetric sound absorption.

Consider for instance the case that the load $\varepsilon_1 = 0.1$ is applied to HR1 with $t = 4 \times 10^{-3}$m, and the load $\varepsilon_2 = 0.08$ is applied to HR2 with $t = 5 \times 10^{-3}$m, as shown in Fig. 6(a). When the incident sound wave enters from the left side of the waveguide, the transmission coefficient T, the reflection coefficient R and the absorption coefficient A of the system are shown in the Fig. 6(b), where the circles are the FE results (using Pressure Acoustic-Thermoacoustic interaction, frequency domain module in COMSOL Multiphysics), and the lines represent the theoretical results. The simulation results are in good agreement with
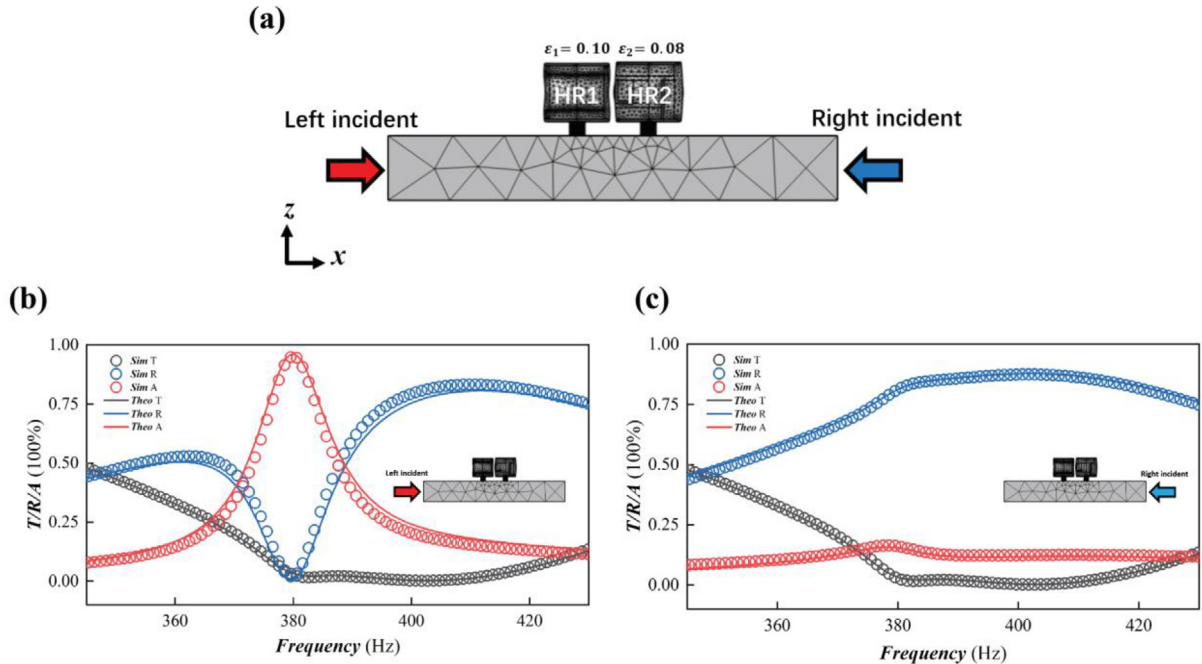

Fig. 6. The system with asymmetric sound absorption: (a) Asymmetric sound absorption device composed of two soft star-shaped HRs. From left to right are HR1 and HR2, respectively, and the compression loads on them are ε_1=0.1 and ε_2=0.08, respectively; (b) The variation of the transmission (T), reflection (R) and absorption (A) coefficients of the system with the incident wave frequency when the sound wave is incident from the left port, which are represented by black, blue and red colors respectively; (c) The variation of T, R and A of the system with the incident wave frequency when the sound wave is incident from the right port. The circles and lines in (b) and (c) represent the results of FE simulation and the theoretical results, respectively.
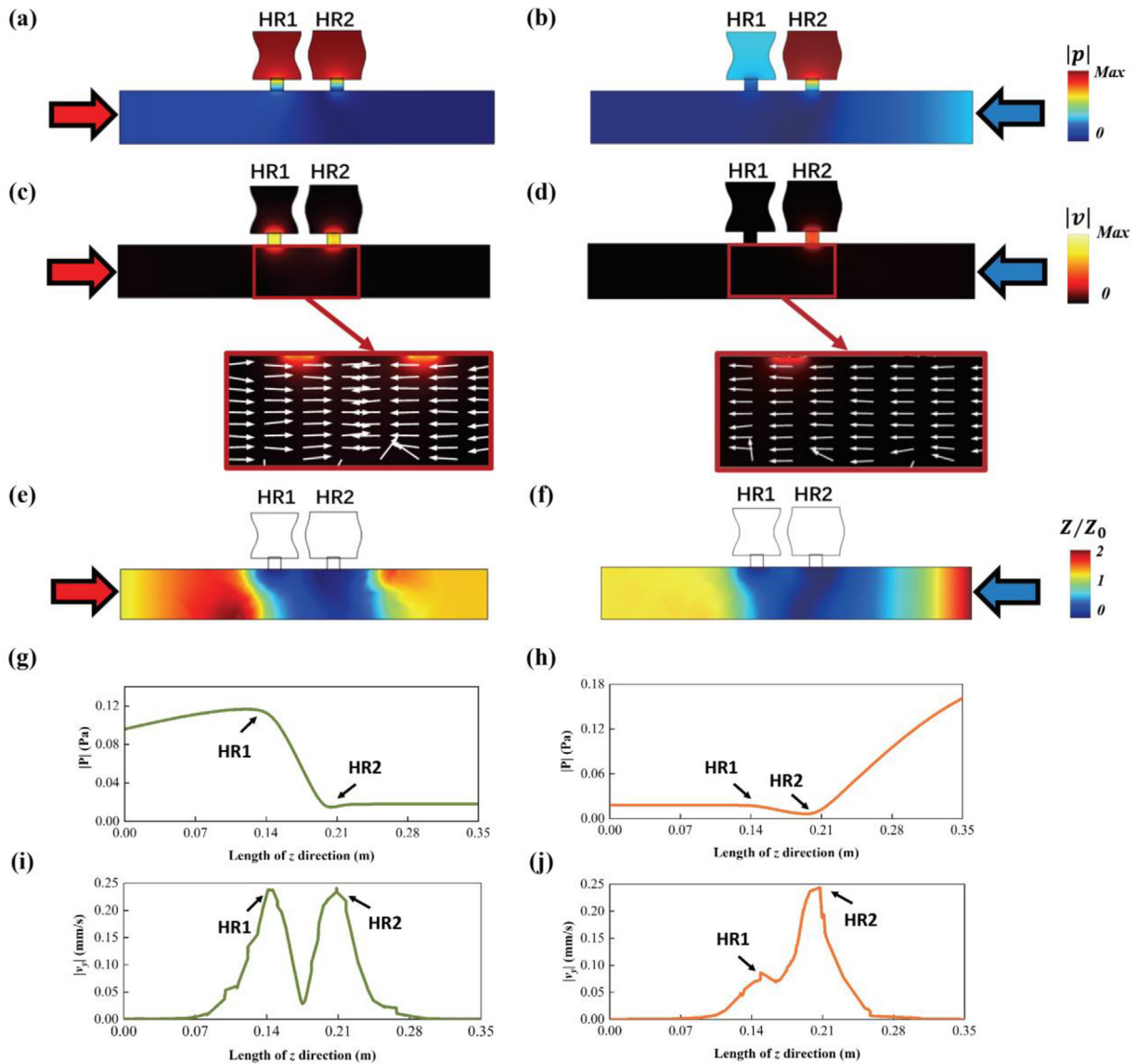
Fig. 7. Sound pressure field, velocity field and distribution of the normalized impedance for different wave incident directions: (a) Sound pressure field $|p|$ for left incidence, and (b) Sound pressure field for right incidence; (c) Velocity field $|v|$ for left incidence, and (d) Velocity field for right incidence, the arrows indicate the velocity directions of the air particles; (e) Distribution of the dimensionalization impedance Z/Z_0 for left incidence, and (f) Distribution of the normalized impedance for right incidence; (g) Variation with the position of the absolute value of sound pressure $|p|$ on the central axis of the waveguide for left incidence, and (h) Variation with the position of the absolute value of sound pressure for right incidence; (i) Variation with the position of the absolute value of particle velocity $|v_y|$ on the central axis of the waveguide under left incidence, and (j) Variation with the position of the absolute value of particle velocity for right incidence.

the theoretical ones. There is an absorption peak at 380Hz, the value of which is about 96.1%, almost approaching 100%. The transmission co-efficient there is about 3.3%, and the reflection is about 0.6%. However, when the sound incident is from the opposite side, as shown in Fig. 6(c), the reflection coefficient reaches 81.2% at the same frequency, which means that most sound energy is reflected rather than absorbed. The transmission coefficient is also 3.3%, and the absorption coefficient is only 15.5%.

Different compression loads can be applied to the soft star-shaped HRs with different thickness to make them have different post-buckling deformation configurations. Then the same incident wave can be inci-dent from different ports to get different sound absorption effects. As indicated in the above example, the incident wave enters from the left side will encounter an almost perfect high absorption. On the contrary, the right one will encounter a high reflection, and a greatly reduced absorption. Thus, the designed system can be tuned mechanically to achieve the asymmetric sound absorption.

From the sound pressure field (Figs. 7(a) and 7(b)) and the velocity field (Figs. 7(c) and 7(d)) at 380Hz, it is found that, when the sound is incident from the left port, the two star-shaped HRs are highly excited at this frequency, and most of the energy is localized inside the neck of HRs, where a high energy density can be identified. Moreover, the velocities of the air particles in the neck are much higher than those in the cavity, which make the energy easily dissipate by the friction. In this regard, the purpose of absorption can be achieved. In addition, from the velocity directions of the air particles (white arrows in Fig. 7(c)), it can be found that the velocity directions near the two HRs are opposite, and the incident wave will be trapped in the tube between the two HRs until the energy is dissipated. This interesting factor also contributes to the near total absorption characteristic. On the contrary, when the sound wave with the same frequency is incident from the right side, only HR2 is excited, as shown in Fig. 7(b). In this latter case, the ve-locity directions of the air particles near the two HRs are the same, as shown in Fig. 7(d). Thus, only a small part of the energy is dissi-
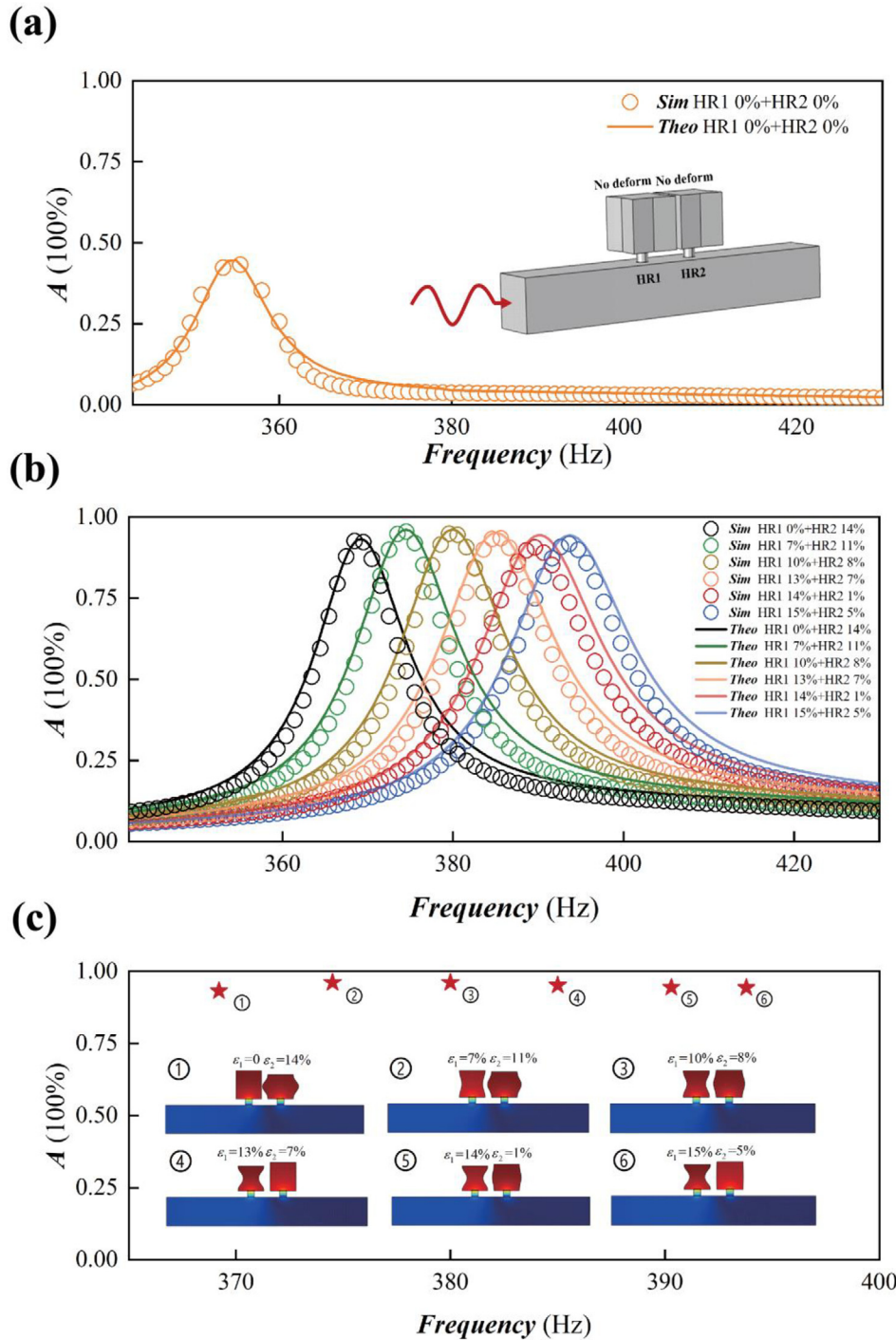
(a)

(b)

(c)

Fig. 8. Sound absorption under different loading combinations: (a) The change of absorption with frequency when both HRs are unloaded; (b) The change of absorption with frequency for different combinations of compression loads on the two HRs; (c) The sound pressure distributions for the load combinations in (b). The circles in (b) represent the results of FE simulation and the lines represent the theoretical results.

pated, and most of the sound wave is reflected, resulting in a small absorption.

This phenomenon can also be explained using the effective acoustic boundary. As we all know, in acoustics, surface impedance is used to measure the "softness" of a boundary. If the surface impedance is close to 0, it can be equivalent to a soft boundary, which means the smallest transmission and the strongest reflection at the boundary. In order to observe the difference in the impedance in the waveguide between two incident directions, the dimensionless impedance at the frequency 380Hz is depicted in Figs. 7(e) and 7(f). The dimensionalization is made in terms of a ratio with respect to the air impedance ($Z_0 = \rho_0 c_0$). Also, the corresponding distributions of the absolute value of sound pressure and

air particle velocity along the central axis of the waveguide are shown in Figs. 7(g), 7(h) and Figs. 7(i), 7(j), respectively. From the results in Figs. 7(e), 7(g) and 7(i), we can see that, when the incident wave is incident from the left side, $Z/Z_0 = 1$ near HR1. That is, the impedance matching condition is satisfied, and the acoustic wave enters into the region between the two HRs. At HR2, $Z/Z_0 = 0$, the sound pressure $|p| = 0$, and the displacement velocity $|v|$ is at the anti-node point, which can be regarded as a soft boundary, where a high reflection exists. Hence the sound energy can be continuously dissipated between the two HRs to achieve a high absorption. However, when the incident wave is incident from the right side, as shown in Figs. 7(f), 7(h) and 7(j), Z/Z_0 at HR2 is equal to 0, $|p|$ is close to 0, and $|v|$ is the maximum, which

Table 1
Specific values of sound absorption under different load combinations.

Compression load on HR1ε_1 (%)	Compression load on HR2ε_2 (%)	Frequency of absorption peak f (Hz)	Absorption at fA (%)
0	14%	369.2 Hz	93.2%
7%	11%	374.5 Hz	96.1%
10%	8%	380 Hz	96.1%
13%	7%	385 Hz	95.1%
14%	1%	390.3 Hz	94.4%
15%	5%	393.8 Hz	94.3%

signifies a soft boundary. Thus, the incident wave encounters a high reflection when it just reaches the position near HR2. In this case, it is difficult for the wave to enter the region between the two HRs, leading to a very low absorption.

5.2. Perfect sound absorption at different frequencies

By combining star-shaped HRs with different thickness and applying different compression loads, we can flexibly tune the acoustic characteristics of the sound absorber to achieve perfect sound absorption at different frequencies. Moreover, based on the characteristics of soft material which can be loaded and unloaded repeatedly, we are able to design an acoustic switch via mechanical loading.

As shown in Fig. 8(a), when both HRs are not loaded, i.e., $\varepsilon_1 = \varepsilon_2 = 0$, and the incident wave is from the right side, there is an absorption peak at 357Hz with the absorption of 42.3%, less than 50%. Moreover, after 365Hz, the absorption is always less than 10%, and there is almost no sound absorption effect.

However, when we apply different compression loads on the top of the two HRs, the absorption can reach more than 90%, as shown in Figs. 8(b) and 8(c). The detailed values are given in Table 1. It can be seen from the results (both numerical and theoretical) that in the range of 365-430Hz, the absorption is less than 10% when no compression load is applied to the HRs. When the appropriate compression loads are applied to the two HRs, both resonators resonate strongly (Fig. 8(c)), and the absorption of the whole system will become more than 90% at some frequencies. It means that we can achieve high sound absorption when the loads are applied on the two HRs, even sound absorption at this frequency is very low when the HRs are unloaded. This kind of sound manipulation can be realized in real time via repeated loading and unloading of soft materials, without the need to change the HRs. In other words, the multi-frequency sound absorption switch can be realized by the means of mechanical control.

Of course, if the number of soft HRs is increased, the tunable frequency range could be further widened, and multi-frequency perfect sound absorption under the specific loading combination could be realized. In addition, the perfect sound absorber can exhibit the phenomenon of asymmetric sound absorption. The reader is referred to Appendix B and Appendix C respectively for some selected results and the discussions.

6. Conclusions

In summary, we have designed a novel kind of star-shaped HR made of soft hyperelastic materials. Placing the soft HRs on the side of acoustic waveguide yields a ventilated and mechanically tunable sound absorber. By applying a compression load on the top of HR, the absorber can exhibit perfect absorption and asymmetric sound absorption at certain frequencies. The following main contributions have been made in this paper:

1) Two kinds of post-buckling mode jumps are found when a compressive load is applied to the top of the soft star-shaped HRs with different thickness. These two post-buckling modes endow the HR cavity

with different volumes and configuration changes under the continuous loading of compression.

2) When two soft star-shaped HRs with different thicknesses are placed on the side wall of the acoustic waveguide, both the theoretical and FE simulation results show that different acoustic characteristics in the sound field would appear under the compression load. In particular, the resonance frequency will change with the load, and the change trend is basically consistent with the variation of the volume of the deforming HR.

3) A ventilated and mechanically tunable acoustic switch is designed by placing two soft star-shaped HRs with different thicknesses on the side wall of the acoustic waveguide. When different compression loads are applied to the two HRs, high sound absorption can be achieved at different frequencies (the sound absorption coefficient is larger than 90%). It is worth mentioning that due to the large deformation property of soft hyperelastic materials, the sound absorption process can be tuned reversibly by mechanical loading and unloading.

4) The soft star-shaped HR absorber also exhibits the characteristic of asymmetric sound absorption. That is, when the incident wave is incident from the different sides of the waveguide, extremely different phenomena, perfect absorption or no absorption, could be observed. Moreover, the phenomenon is also mechanically tunable.

The design presented in this work combines acoustic control with mechanical means, makes the whole control process more feasible and flexible, and widens the application range of acoustic devices.

Declaration of Competing Interest

The authors declare that they have no known competing financial interests or personal relationships that could have appeared to influence the work reported in this paper.

Author statement

We the undersigned declare that this manuscript is original, has not been published before and is not currently being considered for publication elsewhere.

We confirm that the manuscript has been read and approved by all named authors and that there are no other persons who satisfied the criteria for authorship but are not listed.

We further confirm that the order of authors listed in the manuscript has been approved by all of us. We understand that the Corresponding Author is the sole contact for the Editorial process. He/she is responsible for communicating with the other authors about progress, submissions of revisions and final approval of proofs

Supplementary materials

Supplementary material associated with this article can be found, in the online version, at doi:10.1016/j.ijmecsci.2021.106695.

References

[1] Yang M, Sheng P. Sound absorption structures: From porous media to acoustic metamaterials. Annual Review of Materials Research 2017;47:83–114.

[2] Sagartzazu X, Hervella-Nieto L, Pagalday J. Review in sound absorbing materials. Archives of Computational Methods in Engineering 2008;15:311–42.

[3] Song J, Bai P, Hang Z, Lai Y. Acoustic coherent perfect absorbers. New Journal of Physics 2014;16:033026.

[4] Duan Y, Luo J, Wang G, Hang ZH, Hou B, Li J, Sheng P, Lai Y. Theoretical requirements for broadband perfect absorption of acoustic waves by ultra-thin elastic meta-films. Scientific Reports 2015;5:1–9.

[5] Leroy V, Strybulevych A, Lanoy M, Lemoult F, Tourin A, Page JH. Superabsorption of acoustic waves with bubble metascreens. Physical Review B 2015;91:020301.

[6] Yang M, Meng C, Fu C, Li Y, Yang Z, Sheng P. Subwavelength total acoustic absorption with degenerate resonators. Applied Physics Letters 2015;107:104104.

[7] Merkel A, Theocharis G, Richoux O, Romero-García V, Pagneux V. Control of acoustic absorption in one-dimensional scattering by resonant scatterers. Applied Physics Letters 2015;107:244102.

[8] Qu S, Sheng P. Minimizing indoor sound energy with tunable metamaterial surfaces. Physical Review Applied 2020;14:034060.

[9] Groby J-P, Lagarrigue C, Brouard B, Dazel O, Tournat V, Nennig B. Enhancing the absorption properties of acoustic porous plates by periodically embedding Helmholtz resonators. The Journal of the Acoustical Society of America 2015;137:273–80.

[10] Romero-García V, Theocharis G, Richoux O, Merkel A, Tournat V, Pagneux V. Perfect and broadband acoustic absorption by critically coupled sub-wavelength resonators. Scientific Reports 2016;6:1–8.

[11] Guo J, Fang Y, Jiang Z, Zhang X. An investigation on noise attenuation by acoustic liner constructed by Helmholtz resonators with extended necks. The Journal of the Acoustical Society of America 2021;149:70–81.

[12] Duan Y, Luo J, Wang G, Hang Z, Hou B, Li J, Sheng P, Lai Y. Theoretical requirements for broadband perfect absorption of acoustic waves by ultra-thin elastic meta-films. Scientific Reports 2015;5:1–9.

[13] Ma G, Sheng P. Acoustic metamaterials: From local resonances to broad horizons. Science Advances 2016;2:e1501595.

[14] Mei J, Ma G, Yang M, Yang Z, Wen W, Sheng P. Dark acoustic metamaterials as super absorbers for low-frequency sound. Nature Communications 2012;3:1–7.

[15] Xiao S, Ma G, Li Y, Yang Z, Sheng P. Active control of membrane-type acoustic metamaterial by electric field. Applied Physics Letters 2015;106:091904.

[16] Chen Y, Huang G, Zhou X, Hu G, Sun C. Analytical coupled vibroacoustic modeling of membrane-type acoustic metamaterials: Membrane model. The Journal of the Acoustical Society of America 2014;136:969–79.

[17] Ma G, Fan X, Sheng P, Fink M. Shaping reverberating sound fields with an actively tunable metasurface. Proceedings of the National Academy of Sciences 2018;115:6638–43.

[18] Ma G, Yang M, Xiao S, Yang Z, Sheng P. Acoustic metasurface with hybrid resonances. Nature Materials 2014;13:873–8.

[19] Shao C, Liu C, Ma C, Long H, Chen K, Cheng Y, Liu X. Multiband asymmetric sound absorber enabled by ultrasparse Mie resonators. The Journal of the Acoustical Society of America 2021;149:2072–80.

[20] Li Y, Assouar BM. Acoustic metasurface-based perfect absorber with deep subwavelength thickness. Applied Physics Letters 2016;108:063502.

[21] Jiang X, Liang B, Li R, Zou X, Yin L, Cheng J. Ultra-broadband absorption by acoustic metamaterials. Applied Physics Letters 2014;105:243505.

[22] Cai X, Guo Q, Hu G, Yang J. Ultrathin low-frequency sound absorbing panels based on coplanar spiral tubes or coplanar Helmholtz resonators. Applied Physics Letters 2014;105:121901.

[23] Jiménez N, Huang W, Romero-García V, Pagneux V, Groby J-P. Ultra-thin metamaterial for perfect and quasi-omnidirectional sound absorption. Applied Physics Letters 2016;109:121902.

[24] Yang M, Chen S, Fu C, Sheng P. Optimal sound-absorbing structures, Materials Horizons 2017;4:673–80.

[25] Gao N, Wu J, Lu K, Zhong H. Hybrid composite meta-porous structure for improving and broadening sound absorption. Mechanical Systems Signal Processing 2021;154:107504.

[26] Long H, Cheng Y, Tao J, Liu X. Perfect absorption of low-frequency sound waves by critically coupled subwavelength resonant system. Applied Physics Letters 2017;110:023502.

[27] Gao N, Wang M, Cheng B, Hou H. Inverse design and experimental verification of an acoustic sink based on machine learning. Applied Acoustics 2021;180:108153.

[28] Groby J-P, Pommier R, Aurégan Y. Use of slow sound to design perfect and broadband passive sound absorbing materials. The Journal of the Acoustical Society of America 2016;139:1660–71.

[29] Fu C, Zhang X, Yang M, Xiao S, Yang Z. Hybrid membrane resonators for multiple frequency asymmetric absorption and reflection in large waveguide. Applied Physics Letters 2017;110:021901.

[30] Long H, Cheng Y, Liu X. Asymmetric absorber with multiband and broadband for low-frequency sound. Applied Physics Letters 2017;111:143502.

[31] Jiménez N, Romero-García V, Pagneux V, Groby J-P. Rainbow-trapping absorbers: Broadband, perfect and asymmetric sound absorption by subwavelength panels for transmission problems. Scientific Reports 2017;7:1–12.

[32] Zhang H, Wang Y, Zhao H, Lu K, Yu D, Wen J. Accelerated topological design of metaporous materials of broadband sound absorption performance by generative adversarial networks. Materials & Design 2021:109855.

[33] Wu X, Au-Yeung KY, Li X, Roberts RC, Tian J, Hu C, Huang Y, Wang S, Yang Z, Wen W. High-efficiency ventilated metamaterial absorber at low frequency. Applied Physics Letters 2018;112:103505.

[34] Xiang X, Wu X, Li X, Wu P, He H, Mu Q, Wang S, Huang Y, Wen W. Ultra-open ventilated metamaterial absorbers for sound-silencing applications in environment with free air flows. Extreme Mechanics Letters 2020;39:100786.

[35] Xu Z, Gao H, Ding Y, Yang J, Liang B, Cheng J. Topology-optimized omnidirectional broadband acoustic ventilation barrier. Physical Review Applied 2020;14:054016.

[36] Li L, Zheng B, Zhong L, Yang J, Liang B, Cheng J. Broadband compact acoustic absorber with high-efficiency ventilation performance. Applied Physics Letters 2018;113:103501.

[37] Yu X, Lu Z, Liu T, Cheng L, Zhu J, Cui F. Sound transmission through a periodic acoustic metamaterial grating. Journal of Sound and Vibration 2019;449:140–56.

[38] Xiao Z, Gao P, Wang D, He X, Wu L. Ventilated metamaterials for broadband sound insulation and tunable transmission at low frequency. Extreme Mechanics Letters 2021;46:101348.

[39] Xiang X, Tian H, Huang Y, Wu X, Wen W. Manually tunable ventilated metamaterial absorbers. Applied Physics Letters 2021;118:053504.

[40] Bertoldi K, Vitelli V, Christensen J, Van Hecke M. Flexible mechanical metamaterials. Nature Reviews Materials 2017;2:1–11.

[41] Gao N, Huang Y, Bao R, Chen W. Robustly tuning bandgaps in two-dimensional soft phononic crystals with criss-crossed elliptical holes. Acta Mechanica Solida Sinica 2018;31:573–88.

[42] Gao N, Li J, Bao R, Chen W. Harnessing uniaxial tension to tune Poisson's ratio and wave propagation in soft porous phononic crystals: an experimental study. Soft Matter 2019;15:2921–7.

[43] Li J, Wang Y, Chen W, Wang Y, Bao R. Harnessing inclusions to tune post-buckling deformation and bandgaps of soft porous periodic structures. Journal of Sound and Vibration 2019;459:114848.

[44] Wang Y, Wang Y, Wu B, Chen W, Wang Y. Tunable and active phononic crystals and metamaterials. Applied Mechanics Reviews 2020;72:040801.

[45] Shan S, Kang SH, Wang P, Qu C, Shian S, Chen ER, Bertoldi K. Harnessing multiple folding mechanisms in soft periodic structures for tunable control of elastic waves. Advanced Functional Materials 2014;24:4935–42.

[46] Wang P, Casadei F, Shan S, Weaver JC, Bertoldi K. Harnessing buckling to design tunable locally resonant acoustic metamaterials. Physical Review Letters 2014;113:014301.

[47] Wang P, Shim J, Bertoldi K. Effects of geometric and material nonlinearities on tunable band gaps and low-frequency directionality of phononic crystals. Physical Review B 2013;88:014304.

[48] Huang Y, Gao N, Chen W, Bao R. Extension/compression-controlled complete band gaps in 2D chiral square-lattice-like structures. Acta Mechanica Solida Sinica 2018;31:51–65.

[49] Chen Y, Wu B, Li J, Rudykh S, Chen W. Low-frequency tunable topological interface states in soft phononic crystal cylinders. International Journal of Mechanical Sciences 2021;191:106098.

[50] Huang Y, Li J, Chen W, Bao R. Tunable bandgaps in soft phononic plates with spring-mass-like resonators. International Journal of Mechanical Sciences 2019;151:300–13.

[51] Zhou W, Su Y, Chen W, Lim C. Voltage-controlled quantum valley Hall effect in dielectric membrane-type acoustic metamaterials. International Journal of Mechanical Sciences 2020;172:105368.

[52] Wu B, Zhou W, Bao R, Chen W. Tuning elastic waves in soft phononic crystal cylinders via large deformation and electromechanical coupling. Journal of Applied Mechanics 2018;85:031004.

[53] Zhou W, Wu B, Muhammad QDu, Huang G, Lü C, Chen W. Actively tunable transverse waves in soft membrane-type acoustic metamaterials. Journal of Applied Physics 2018;123:165304.

[54] Wang Y, Li J, Fu Y, Bao R, Chen W, Wang Y. Tunable guided waves in a soft phononic crystal with a line defect. APL Materials 2021;9:051124.

[55] Deng B, Yu S, Forte AE, Tournat V, Bertoldi K. Characterization, stability, and application of domain walls in flexible mechanical metamaterials. Proceedings of the National Academy of Sciences 2020;117:31002–9.

[56] Kochmann DM, Bertoldi K. Exploiting microstructural instabilities in solids and structures: from metamaterials to structural transitions. Applied Mechanics Reviews 2017;69.

[57] Su T, Liu J, Terwagne D, Reis PM, Bertoldi K. Buckling of an elastic rod embedded on an elastomeric matrix: planar vs. non-planar configurations. Soft Matter 2014;10:6294–302.

[58] Al-Azzawi AS, Kawashita LF, Featherston CA. Buckling and postbuckling behaviour of Glare laminates containing splices and doublers. Part 2: Numerical modelling. Composite Structures 2017;176:1170–87.

[59] Cui S, Harne RL. Soft materials with broadband and near-total absorption of sound. Physical Review Applied 2019;12:064059.

[60] Song BH, Bolton JS. A transfer-matrix approach for estimating the characteristic impedance and wave numbers of limp and rigid porous materials. The Journal of the Acoustical Society of America 2000;107:1131–52.

[61] Kergomard J, Garcia A. Simple discontinuities in acoustic waveguides at low frequencies: critical analysis and formulae. Journal of Sound and Vibration 1987;114:465–79.

[62] Dubos V, Kergomard J, Khettabi A, Dalmont J-P, Keefe D, Nederveen C. Theory of sound propagation in a duct with a branched tube using modal decomposition. Acta Acustica united with Acustica 1999;85:153–69.

[63] Li J, Wen X, Sheng P. Acoustic metamaterials. Journal of Applied Physics 2021;129:171103.

[64] Yang M, Li Y, Meng C, Fu C, Mei J, Yang Z, Sheng P. Sound absorption by subwavelength membrane structures: A geometric perspective. Comptes Rendus Mécanique 2015;343:635–44.